



Synergistic effect in ultrafine PtNiP nanowires for highly efficient electrochemical hydrogen evolution in alkaline electrolyte

Qian Chen^{a,1}, Bo Wei^{a,1}, Yi Wei^b, Pengbo Zhai^a, Wei Liu^a, Xiaokang Gu^a, Zhilin Yang^a, Jinghan Zuo^a, Ruifeng Zhang^{a,*}, Yongji Gong^{a,*}

^a School of Materials Science and Engineering, Beihang University, 100191, Beijing, China

^b State Key Laboratory of Organic-Inorganic Composites, Beijing Key Laboratory of Electrochemical Process and Technology for Materials, Beijing University of Chemical Technology, Beijing 100029 China

ARTICLE INFO

Keywords:

Hydrogen evolution reaction
PtNiP nanowires
Synergistic effect
Alkaline electrolyte

ABSTRACT

Platinum-based catalysts play an important role in electrochemical hydrogen evolution reaction, which is a renewable and clean way to produce H₂. Herein, we have successfully synthesized the ultrafine PtNiP NWs with diameter less than 5 nm via a simple two-step hydrothermal reaction method. Impressively, the PtNiP NWs exhibit one of the best electrocatalytic activity toward HER under alkaline conditions, which can reach current density of 500 mA cm⁻² only at the -0.153 V vs RHE with Tafel slop of only 30 mV dec⁻¹. The DFT calculation results show synergistic effect of Pt, Ni and P atoms, where Ni atoms are conducive to the adsorption of H₂O and P atoms are helpful for the dissociation of H₂O, significantly improving kinetic processes of hydrogen evolution reaction. This work could be instructive and meaningful to design highly efficient and stable HER catalyst in alkaline condition for practical applications.

1. Introduction

Hydrogen, considered as a renewable and clean energy, has played an increasingly important role as the substitutes of traditional fossil fuels [1,2]. Among various hydrogen production methods, more and more attention is paid to electrochemical hydrogen evolution reaction (HER), which is the cathode reaction in water electrolysis because of high product purity and the recycle of water [3]. Generally speaking, HER takes place more easily in acidic solutions because of the faster kinetics to convert H⁺ rather than H₂O to H₂. However, in the process of industrial electrochemical hydrogen production, the electrolyte solution is often alkaline for a better performance of oxygen evolution reaction (OER). This results in a higher water decomposition voltage and consumes more energy due to the large energy dissociation barrier of water molecules into H₂ under alkaline conditions. Currently, platinum (Pt) is a widely used commercial catalyst for HER, but its application is limited by the high price and scarcity. Thus, a lot of Pt-free catalysts such as metal oxides [4–6], metal sulfide [7–10], metal nitrides [11,12], metal phosphide [13], MXene [14–17], LDH [18–20], and metal-free catalysts [21,22] have been widely studied as effective substitutes to reduce the

cost of the catalyst. Nevertheless, there is still a significant gap in performance compared to the present state of Pt catalysts and most Pt-free catalysts only work well in acidic condition [23]. Therefore, it is still recognized that Pt is most widely used catalyst for its superior HER performance [24]. Further improving Pt based catalysts HER performance in alkaline condition plays an important role in saving energy for industrial application.

Using nanostructured Pt and non-noble metal doping are two effective strategies to further improve the ability for water dissociation and to reduce the consumption of Pt [25–27]. Among the various kinds of Pt nanostructures, the ultrafine nanowires have attracted increasing attentions due to their large surface area and high aspect ratios, which can provide numerous catalytic sites [28–31]. Furthermore, Pt surface can be engineered by various transition metals, such as Fe, Co and Ni, to drive the d-band center away from the Fermi level, which directly weakens hydrogen adsorption energies and facilitates the release of H₂ in the HER [32,33]. Although great improvements have been achieved by these strategies, the performance of Pt based catalysts is still inferior in alkaline electrolyte than acidic electrolyte.

Herein, PtNiP nanowires (PtNiP NWs) are synthesized by

* Corresponding authors.

E-mail addresses: zrf@buaa.edu.cn (R. Zhang), yongjigong@buaa.edu.cn (Y. Gong).

¹ These authors contributed equally to this work.

phosphorizing PtNi NWs, making phosphorus atoms distributing on the nanowires evenly. Based on our DFT calculation, we found that Ni atoms are conducive to the adsorption of water molecules, P atoms facilitate the adsorption of OH*, which can accelerate the diffusion of H* to Pt atoms and then the generation of H₂. Due to the synergistic effect of Pt, Ni and P elements, PtNiP NWs have exceptional HER performance in alkaline condition, which is better than the commercial Pt/C. Specifically, PtNiP NWs delivers unprecedented low overpotential of 9 mV at current densities of 10 mA cm⁻² and 44 mV at 100 mA cm⁻² in 1 M KOH with Tafel slop of only 30 mV dec⁻¹, which is one of the best performances among all the available HER electrocatalysts in alkaline condition. Moreover, due to the excellent kinetic, PtNiP NWs can reach current densities of 500 mA cm⁻² only at overpotential of 153 mV, comparable to the performance of Pt in acidic electrolyte. Besides, it exhibits a HER current density of 6.27 mA ug_{Pt}⁻¹ at an overpotential of 70 mV, which is 5.59 times that of the commercial Pt/C catalyst at the same overpotential.

2. Experimental section

2.1. Synthesis of PtNi NWs

The PtNi NWs were synthesized by a hydrothermal method. Typically, ammonium chloroplatinate ((NH₄)₂PtCl₆, 70 mg), potassium hydroxide (KOH, 500 mg) and nickel (II) chloride hexahydrate (NiCl₂·6H₂O, 20 mg) were added into a mixed solution consisting of ethylene glycol (EG, 9 mL) and N, N-dimethylformamide (DMF, 3 mL). After stirring at 50 °C for 3 h, the resultant homogeneous yellow solution was transferred into a Teflon-lined stainless-steel autoclave under 170 °C for 8 h [34]. After cooling down to room temperature, the production was collected by filtration, washing three times with the ethanol/DI water mixture, and then the black production was dried out at room temperature.

2.2. Synthesis of PtNiP NWs and PtNiP-Ni₂P NWs

Typically, 30 mg PtNi NWs and 3 mg phosphorus powder were dissolved in 13 mL EG under magnetic stirring. the resultant homogeneous yellow solution was transferred into a Teflon-lined stainless-steel autoclave under 180 °C for 8 h. After cooling down to room temperature, the production was collected by filtration, washing three times with the ethanol/ DI water mixture, and then the black production was dried out at room temperature. PtNiP-Ni₂P NWs were obtained through same synthesis procedure, except that the addition amount of phosphorus powder was 10 mg.

2.3. Characterization

X-ray powder diffraction (XRD) patterns were obtained on X-ray diffractometer (Rigaku D/max2500PC) equipped with Cu Kα radiation for 2-Theta range of 5°–90°. FE-SEM (Hitachi SU8020) observations were used to characterize the morphology with an energy dispersive spectrometry (EDS). TEM, HRTEM, and EDS samples were examined under the JEOL JEM-2100 F. STEM characterization was performed on an aberration-corrected Nion HERMES-100 under the accelerating voltage of 100 kV, with a probe-forming angle of 30 mrad. The collection angle of STEM-HAADF imaging is 92–210 mrad. The EELS mappings were acquired under the same condition with a collection angle of 92 mrad and a probe current of ~60 pA. Detailed chemical compositions were analyzed by X-ray photoelectron spectroscopy (XPS) on an ESCA-LAB 250 photoelectron spectrometer (Thermo Fisher Scientific) using a monochromatic Al Kα X-ray beam (1486.6 eV). All binding energies were referenced to the C 1s peak (284.6 eV). The Nickel concentrations were conducted on the Agilent 7500ce ICP-OES. The X-ray absorption fine structure data were collected at 1W1B station in Beijing Synchrotron Radiation Facility (BSRF). The storage rings of BSRF were operated

at 2.5 GeV with a maximum current of 250 mA. All samples were pelletized as disks of 13 mm diameter using graphite powder as a binder. The EXAFS oscillations χ(k) were extracted and analyzed by the Demeter software package. The pore size distribution was determined using density functional theory (DFT) model for slit shaped and cylindrical pores.

2.4. Electrochemical measurements

The electrochemical test was performed on the CHI760E electrochemical workstation (Chen hua, shanghai) using a three-electrode system in 1.0 M KOH aqueous solution with carbon rod and Ag/AgCl as the counter and reference electrodes. Typically, the catalyst dispersion was prepared by mixing 1 mg catalyst and 1 mg carbon black in 1 mL of solution, consisting of 700 μL water, 250 μL ethanol and 50 μL Nafion solution. Followed by ultrasonication for 1 h to form a homogeneous catalyst ink, 10 μL of the catalyst ink was loaded onto a glassy-carbon rotating disk electrode (RDE) (diameter: 5 mm, area: 0.196 cm²) and dried at room temperature for at least 3 h (Pt loading amount of 30.6 μg cm⁻²). Notably, to control the Pt loading amount, 5 mg 10% Pt/C was added to the catalyst dispersion (25.5 μg cm⁻²). The cyclic voltammetry (CV) was carried out with a scan rate of 50 mV s⁻¹. The catalysts were cycled about 50 cycles until a stable cyclic voltammetry curve was developed before linear sweep voltammetry (LSV) test. The catalytic activity was measured by LSV with a scan rate of 30 mV s⁻¹ and the rotation rate of RDE was 1600 rpm. Electrochemical impedance spectroscopy (EIS) measurements were conducted at -100 mV vs. RHE in the frequency range from 10 kHz to 0.01 Hz. The polarization curves were corrected by iR compensation. The correction was performed according to the following equation:

$$E_{\text{correct}} = E_{\text{measured}} - iR_s$$

where the E_{correct}, E_{measured}, i and R_s are the iR-corrected potential, the measured potential versus RHE, the current, and the internal resistance acquired by the EIS, respectively.

The electrochemical active surface area (ECSA) was determined by integrating the charge passed during the hydrogen desorption by the cyclic voltammetry (CV) with a sweep rate of 50 mV s⁻¹ at room temperature in nitrogen-saturated 1.0 M KOH solution. The durability tests were performed in 1.0 M KOH solution using chronopotentiometry (CP) test method.

2.4.1. TOF calculation

In this method, the hydrogen desorption peak, represents electron transfer quantity (Q_H). The number of active sites:

$$n = \frac{Q_H}{2 * F}$$

TOF can be calculated with the following equation:

$$TOF(s^{-1}) = \frac{I}{2 * F * n}$$

Where the number 2 means two electrons to generate one hydrogen molecule, F is Faraday constant (96,485 C mol⁻¹), n is the number of active sites (mol), I (A) is the measured current during linear sweep measurement at a specific overpotential.

2.5. DFT models and calculations

The spin-polarized DFT calculations were performed using the Vienna Ab-initio Simulation Package (VASP) with the projector-augmented wave pseudopotentials (PAW) and Perdew-Burke-Ernzerhof (PBE) generalized gradient approximation (GGA). The Pt (1 1 1), Pt₃Ni (1 1 1) and Pt₃NiP (1 1 1) surfaces were modeled by four-layer atomic slabs with a 3 × 3 supercell and the atoms in the top three

layers were relaxed, while the rest of the atoms were constrained. The vacuum layer thickness in the *z*-direction was set as 20 Å to avoid artificial interactions between periodic images. A $5 \times 5 \times 1$ k-mesh grid was used for geometry optimization and the kinetic energy cutoff was 520 eV and the convergence tolerance for residual force and energy were set to $0.01 \text{ eV } \text{\AA}^{-1}$ and 10^{-5} eV on each atom.

To determine the transition state for water dissociation and HER on the Pt (1 1 1), Pt₃Ni (1 1 1) and Pt₃NiP (1 1 1) surfaces, we employed the climbing image nudged elastic band method (CI-NEB). The free energy diagram for HER was obtained by calculating the change of the free energy with a hydrogen atom adsorbed on the surface following the computational hydrogen electrode model, and the hydrogen adsorption free energy ΔG_{H^*} is determined as

$$\Delta G_{\text{H}^*} = \Delta E_{\text{H}} + \Delta E_{\text{ZPE}} - T\Delta S_{\text{H}},$$

where $\Delta E_{\text{H}} = E_{\text{H}^*} - E_{\text{H}_2} - \frac{1}{2}E_{\text{H}_2}$ is the energy difference of the surface with and without the H adsorbate, respectively, E_{H_2} is the total energy of a gaseous H₂; $\Delta E_{\text{ZPE}} = E_{\text{ZPE}}^{\text{H}} - E_{\text{ZPE}}^{\text{H}_2} - \frac{1}{2}E_{\text{ZPE}}^{\text{H}_2}$ is the difference in the zero-point energy between the adsorbed H* atom and the gaseous H₂; $\Delta S_{\text{H}} \approx -\frac{1}{2}S_{\text{H}_2}^0$ is the difference in entropy.

3. Results and discussion

The PtNiP NWs were synthesized by a simple two-step solvent thermal reaction. As illustrated in Fig. 1 (Details in Experimental Section), to synthesize ultrafine PtNi NWs, ammonium chloroplatinate and nickel chloride hexahydrate were first dissolved in an alkaline solution consisting of ethylene glycol and N, N-dimethylformamide (DMF). Then the mixture was transferred to a Teflon-lined stainless-steel autoclave and heated at 170 °C for 8 h. The PtNi NWs were obtained after vacuum drying overnight. Based on the previous studies, the reaction time plays an important role in the formation process and growth mechanism of Pt-based nanowires. With the reaction time increasing, coalescence of nanoparticles in the aligned direction occurred to form nanorods and eventually nanowires. Besides, the amine species produced from the reaction of DMF and KOH during hydrothermal process would adsorb on Pt nanostructures and induce the formation of Pt nanowires [35–38]. In the phosphating process, the PtNi NWs and phosphorus powder was dispersed in ethylene glycol and transferred into a Teflon-lined stainless-steel autoclave under 180 °C for 8 h. Ultrafine PtNiP NWs were obtained via vacuum assisted filtration and vacuum drying overnight.

The X-ray powder diffraction (XRD) patterns of the PtNi and PtNiP NWs are presented in Fig. 2a. The peaks of both PtNi and PtNiP NWs are similar to pure Pt, indicating the formation of Pt-based alloys. The PtNiP NWs show peaks shift to higher values compared with those from PtNi NWs, confirming the lattice constant change due to P doping. Furthermore, when a larger dose of phosphorus powders were added during

synthesis process, the peaks of Ni₂P would appear and the product was denoted as PtNi-Ni₂P NWs (Fig. S1). Fig. 2b–c show scanning electron microscope (SEM) images and transmission electron microscopy (TEM) images of PtNiP NWs, revealing that these nanowires usually consist of bundles of ultrafine nanowires with diameter of less than 5 nm. Since there is no ultrasonic dispersion process, the diameter of nanowires in SEM images, consisting of bundles of ultrafine nanowires, is larger than that in TEM images. High-resolution TEM (HRTEM) images of these individual nanowires in Fig. 2d show clear lattice fringes with an interplanar distance of approximately 0.22 nm of Pt (1 1 1) planes, and its corresponding Fourier diffractogram patterns are shown in Fig. 2e. The result indicates that the nanowires are composed of homogeneous PtNi alloys, rather than a heterostructure of the two individual materials. Notably, the morphology of PtNiP NWs did not change obviously after phosphating process compare to PtNi NWs (Fig. S2–S4). Due to the overlapping peaks of Pt (M 2.048 keV) and P (Kα 2.013 keV), it is hard to figure out the element distribution in PtNiP NWs by energy dispersive spectrometer (EDS) test. Therefore, high-angle annular dark-field scanning transmission electron microscopy (HAADF-STEM) and electron energy loss spectroscopy (EELS) were applied to reveal the presence of P in the nanowires (Fig. S5). As shown in Fig. 2f (i–iv), both of Ni and P are distributed over the whole nanowires. Moreover, there are no obvious particles on the surface of nanowires, indicating that P atoms are evenly distributed on nanowires instead of forming metal phosphide nanoparticles.

X-ray photoelectron spectroscopy (XPS) was carried out to further explore the valence of existing elements and the chemical bonds. For PtNi NWs, the peaks located at 853.0 and 870.0 eV are attributed to the Ni⁰ while 856.1 and 874.0 eV are contributed from the oxidized state of Ni (Fig. 3a). Similarly, the XPS result of Pt in Fig. 3b reveals the coexistence of a mass of Pt⁰ and little number of Pt²⁺ in PtNi NWs. The positive valence of Ni and Pt can be explained by surface oxidation in air of the ultrafine NWs. As for PtNiP NWs, the binding energies of 853.2 and 870.2 eV are assigned to Ni^{δ+} which is caused by the charge transfer of Ni after P doping [39]. Furthermore, the ratio of low valence Ni/high valence Ni is higher than that of PtNi NWs, indicating that part of oxidized Ni²⁺ is converted into Ni^{δ+} after phosphating. Meanwhile, the peaks of Pt in PtNiP move up to higher binding energies compared to those in PtNi NWs, confirming electron transfer from Pt to P and Pt active centers with more vacant d-orbitals are created, which is beneficial for the HER activity [40,41]. The XPS result of P is also given in Fig. 3c, which can prove the presence of negative charged P^{δ-} [42,43]. Besides, the main form of P is the oxidation state, which is probably due to the formation of phosphate adsorbed on the surface of nanowires [44]. XPS full spectrum in Fig. 3d shows that PtNiP nanowires are consist of Pt 78.9 wt%, Ni 8.23 wt% (Pt:Ni atomic ratio≈3:1), O 9.37 wt% and P 3.51 wt%, and inductive coupled plasma-atomic emission spectrometer (ICP-AES) test was further carried out to confirm the

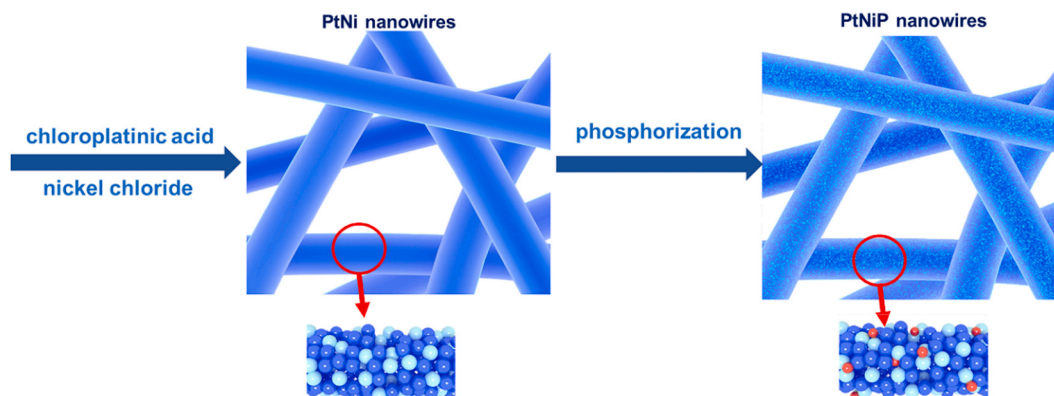


Fig. 1. The synthesis schematic diagram of PtNiP NWs (blue, cyan, and red spheres represent platinum, nickel, and phosphorus atoms, respectively).

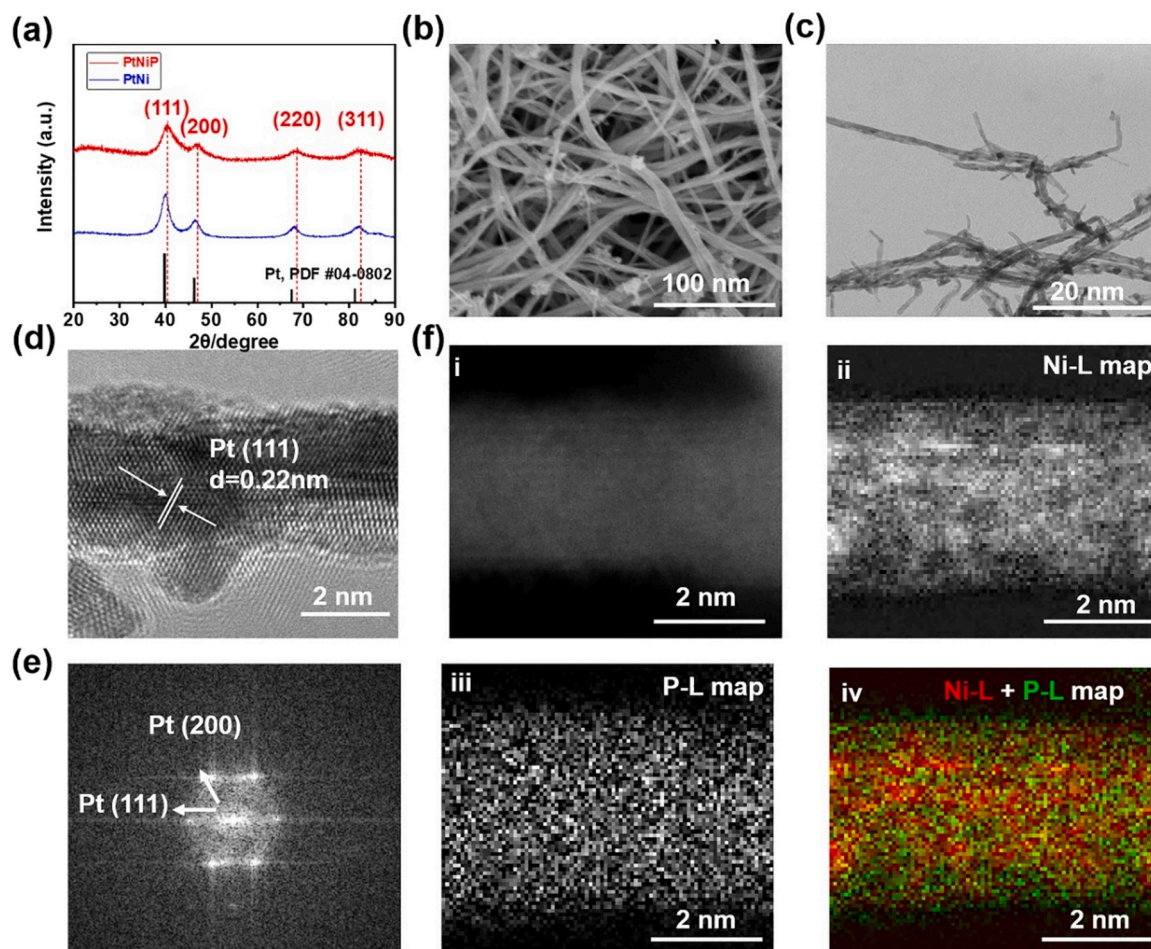


Fig. 2. (a) XRD pattern of PtNi NWs and PtNiP NWs. (b) SEM images of PtNiP NWs. (c) TEM images of PtNiP NWs magnifications. (d) HRTEM image of PtNiP NWs. (e) Corresponding Fourier diffractogram for Fig. 2d. (f) EELS chemical composition maps of PtNiP NWs from the area in the HADDF-STEM image.

element content. It turned out that Pt 77.3 wt%, Ni 9.7 wt%, O 9.2 wt% and P 3.8 wt% in PtNiP NWs, which is consistent with the XPS results. X-ray absorption near edge structure (XANES) and the Fourier transforms of extended X-ray absorption fine structure spectra (FT-EXAFS) PtNi NWs, PtNiP NWs, and Pt foil for the Pt L3-edge are given in Fig. 3e-f. The intensity of the white line peak at about 11.56 keV for the PtNi NWs and PtNiP NWs are similar to that of the Pt foil, indicating the dominating metallic state of Pt in the PtNi NWs structure, which is consistent with the XPS results of the PtNi NWs. The main peak in the Pt L3-edge FT-EXAFS spectra represents the nearest coordination shells of Pt atoms, which was well reproduced through a fitting using Pt-P, Pt-Ni and Pt-Pt paths (Fig. S6 and Table S1). The shorter radial distance of the main peak in the PtNiP NWs suggests the shorter bond length than that of the Pt foil, owing to the heteroatomic interaction in binary alloy [45, 46].

The HER performance of PtNiP NWs was investigated by using linear sweep voltammetry (LSV) method at a scan rate of 30 mV s^{-1} in 1 M KOH at room temperature after iR correction with PtNi NWs and commercial Pt/C as control group. The measurement was tested on rotating disk electrode (RDE) with rotate speed 1600 RPM and calibrated by the reversible hydrogen electrode (RHE). Different catalysts with the same amount of Pt were mixed with commercial carbon black with the aid of sonication (See details in experimental section). Fig. 4a displays the LSV curves of PtNiP, PtNi and commercial Pt/C. It is clearly that PtNiP NWs own the best performance no matter in small or large current in alkaline condition. The overpotential of PtNiP NWs is only 9 mV at the current density of 10 mA cm^{-2} , which is better than PtNi NWs (19 mV) and commercial Pt/C catalyst (31 mV). More significantly, at a large current

density of 100 mA cm^{-2} , the overpotential of PtNiP NWs (44 mV) is still much lower than PtNi NWs (109 mV) and Pt/C (134 mV). Particularly, the PtNiP NWs can reach a current density of 500 mA cm^{-2} at the -0.153 V vs RHE, which is obviously advantageous comparing to the other catalysts. Even without RDE test (Fig. S7), the PtNiP NWs also exhibit an impressive overpotential of 10 mV at the current density of 10 mA cm^{-2} . Moreover, PtNiP NWs still has the best performance compare to PtNi and Pt/C in acidic condition (Fig. S8). The overpotential of Ni₂P and PtNiP-Ni₂P are 294 mV and 25 mV at the current density of 10 mA cm^{-2} (Figs. S9 and S10), indicating that Ni₂P phase is not beneficial to improve HER activity in the alkaline condition. And a less P dose sample of PtNiP NWs (denoted as PtNiP-L) by adding 1 mg phosphorus powder during synthetic process, and the HER performance was further tested. As shown in Fig. S11a, the overpotential of PtNiP-L NWs is 78 mV at the current density of 50 mA cm^{-2} , which is much worse than that of PtNiP NWs (43 mV). Moreover, PtNiP-L NWs exhibit a higher Tafel slope (91.2 mV dec^{-1}) compared to PtNiP-L NWs (36.5 mV dec^{-1}), indicating that PtNiP-L NWs own poor HER performance (Fig. S11b). It is fair to infer that smaller P dose will lead to less active sites with inferior HER performance. To compare the properties of different Pt catalysts more intuitively, the mass activity (MA) is given by Fig. 4b. The PtNiP NWs still have much lower overpotential (24 mV) than PtNi NWs (50 mV) and Pt/C (72 mV) at $1 \text{ mA ug}_{\text{Pt}}^{-1}$. At the overpotential of 70 mV (Fig. 4c), the current density and mass activity of PtNiP NWs are $223.59 \text{ mA cm}^{-2}$ and $6.27 \text{ mA ug}_{\text{Pt}}^{-1}$, which is 4.84 and 5.59 times higher than commercial Pt/C catalyst, respectively. In addition, a series of PtNiP NWs were synthesized with different Pt content, which were determined by XPS results to be 90 wt%, 78 wt%, 61 wt%

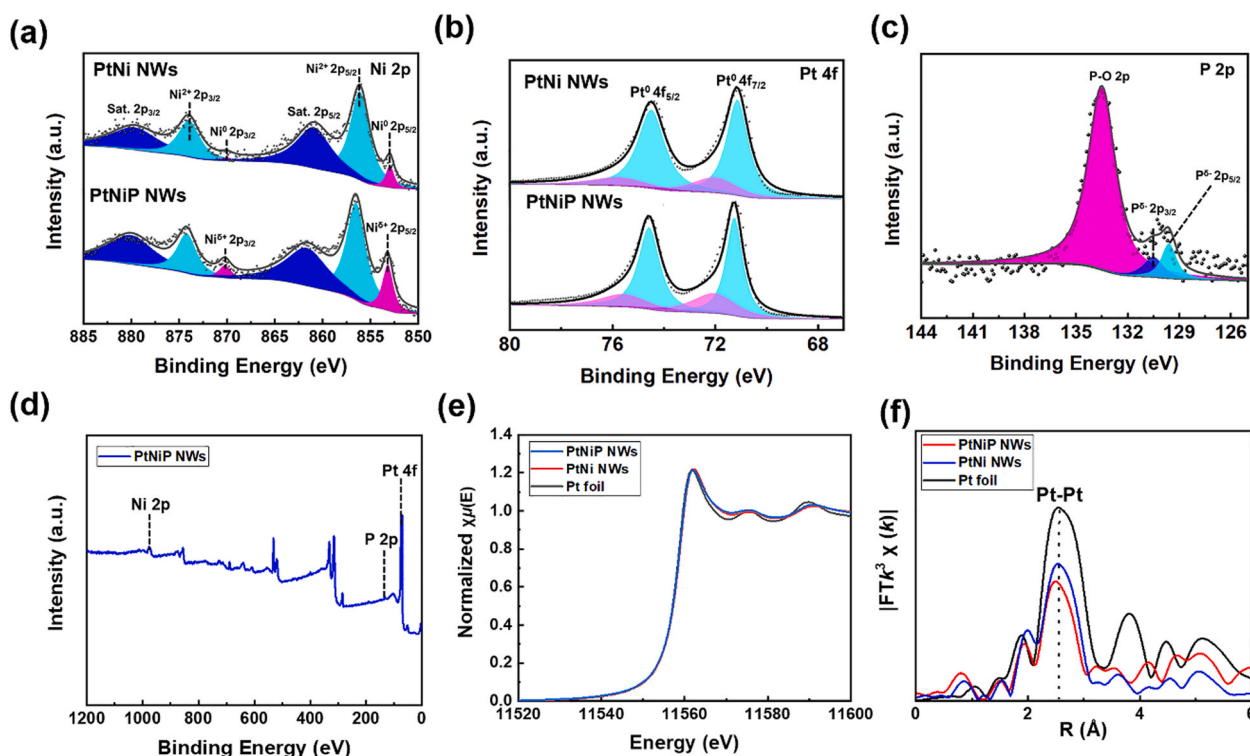


Fig. 3. XPS and XANES characterization. (a) Ni 2p XPS spectra. (b) Pt 4f XPS spectra. (c) P 2p XPS spectra. (d) XPS full spectrum of PtNiP NWs. (e) The XANES and (f) The Fourier transforms of EXAFS spectra of PtNi NWs, PtNiP NWs, and Pt foil for the Pt L3-edge.

and 46 wt%, and denoted as PtNiP-1, PtNiP-2, PtNiP-3 and PtNiP-4, respectively. The SEM images of the four samples (Fig. S12) indicate that with the decrease of Pt content, increasing nickel oxide particles can be observed on the surface of nanowires due to the excessive nickel, which reduce the overall electrocatalytic activity. Fig. S13 displays the results of high resolution XPS for Pt 4 f of PtNiP-X (X = 1–4). It is obviously that as the content of Pt increases, the binding energy exhibits a shift toward higher position due to the alloying between Pt and Ni, which leads to a downward shift of its d-band center and improve the catalytic activity. The HER performances of samples are shown in Fig. S14. It is ideal to achieve high current density with low platinum content in NWs. Evidently, PtNiP-2 NWs exhibit optimal HER activity, with a current density of $143.08 \text{ mA cm}^{-2}$ and a mass activity of $2.86 \text{ mA } \mu\text{g}_{\text{Pt}}^{-1}$ at the overpotential of 70 mV. Besides, the stability test reveals that higher Pt content contribute to a better stability and lower overpotential. The electrochemically active surface area (ECSA) was determined by integrating the current passed during the hydrogen desorption in cyclic voltammetry (Fig. S15). It turns out that the ECSA of three different samples are almost the same (Fig. S16). The turnover frequency (TOF) value of PtNiP NWs, calculated by using the number of Pt active sites (Figs. 4d and S17), can reach as high as $128.87 \text{ H}_2 \text{ S}^{-1}$, which is 21.9 times higher than that of Pt/C catalyst. Thus, it can conclude that the better performance of PtNiP NWs can be attributed to the more active catalytic sites rather than more catalytic sites.

It is generally believed that basic HER process includes the formation step of adsorbed hydrogen species ($\text{H}_2\text{O} + \text{e}^- \rightarrow \text{H}_{\text{ad}} + \text{OH}^-$, Volmer step) and the desorption step of adsorbed hydrogen to form hydrogen molecules ($\text{H}_{\text{ad}} + \text{H}_2\text{O} + \text{e}^- \rightarrow \text{H}_2 + \text{OH}^-$, Heyrovsky step or $2\text{H}_{\text{ad}} + 2\text{e}^- \rightarrow \text{H}_2$, Tafel step). By analyzing the Tafel curve, we can obtain the rate-determining step and the main reaction mechanism during HER process. To better illustrate the reaction mechanism, the Tafel curves are divided into two segments (Fig. 4e and f). In the range of low current density, the rate-determining step of reaction is production of hydrogen molecules. The Tafel slope of PtNiP NWs, PtNi NWs and Pt/C are 30.5, 40.0, 45.0 mV dec^{-1} , indicating that hydrogen is mainly produced by

Volmer-Tafel mechanisms for PtNiP NWs while Volmer-Heyrovsky mechanisms for the others [47,48]. Particularly, at large current density around 100 mA cm^{-2} , the Tafel slope of PtNi NWs and Pt/C are 98.0 mV dec^{-1} and $141.7 \text{ mV dec}^{-1}$, indicating that rate-determining step turns into the production of adsorbed hydrogen species. The sluggish Volmer step causes the lack of adsorbed hydrogen species and restricts the kinetics of the whole reaction [49]. Luckily, PtNiP NWs exhibits an extremely low Tafel slope of 55.9 mV dec^{-1} around 100 mA cm^{-2} . The possible mechanism for the superior performance of PtNiP NWs is that the active sites own a lower energy barrier for the dissociation of H_2O molecule, which can accelerate the Volmer step and provide enough adsorbed hydrogen species for subsequent reaction. Moreover, electrochemical impedance spectroscopy (EIS) was used to explore the charge transfer kinetics between the electrode and electrolyte during the reaction. As shown by the Nyquist plots (Fig. 4g), it is obvious that circle arcs for PtNiP NWs are smaller, meaning lower resistances. Furthermore, an equivalent circuit model (Table S2) constituting of subsistent resistance in series was used to simulate the EIS data. The reason for solution resistance (R_s) of PtNiP NWs is larger than the others is that a lot of H_2 bubbles are adsorbed on the electrode surface during the test, which affect the connection between the electrolyte and electrode. Benefitting from the excellent conductivity of PtNiP NWs and electrocatalytic kinetics performance, the fitted values of containing resistance (R_c) and reaction charge transfer process R_{CT} are only 0.34 ohm and 5.14 ohm, which is much smaller than PtNi NWs and Pt/C. Besides, the long-term durable test (Fig. 4h) was carried by chronopotentiometry (CP) test at the current density of 50 mA cm^{-2} . After 60 h of continuous electrolysis, PtNiP NWs maintained high electrocatalytic activity and showed no obvious potential increase (varies from -0.044 to -0.073 V vs RHE). Moreover, We further provided an in-depth insight of the catalytic durability for these catalysts by examining their morphology and composition changes after 60 h stability tests. Fig. S18a shows that the morphology of the PtNiP NWs can be well maintained after stability test. Furthermore, the Pt/Ni atomic ratio increased from 3:1–88:12 after the stability test due to the inevitable

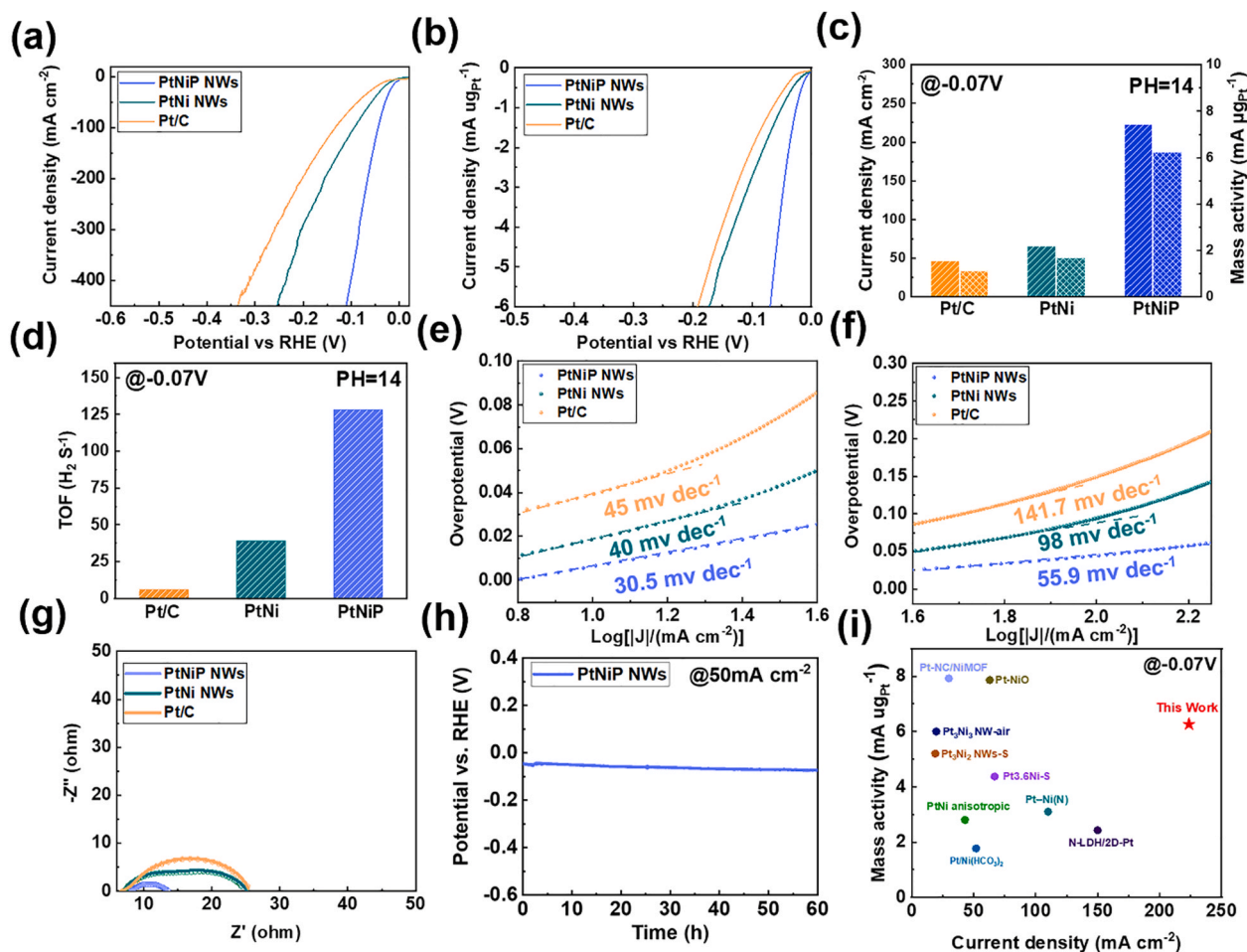


Fig. 4. (a) Current density and (b) mass activity LSV curves of PtNi NWs, PtNiP NWs and 10% Pt/C in 1 M KOH. (c) HER performance and (d) TOF histograms at -0.07 V versus RHE. (e) and (f) Tafel plots of PtNi NWs, PtNiP NWs and 10% Pt/C. (g) EIS (presented in scatter plot) curves and the related fitted results (lines) of PtNi NWs, PtNiP NWs and 10% Pt/C at a potential of -0.1 V versus RHE. (h) Chronopotentiometric curve for HER stability of PtNiP NWs in 1 M KOH at a current density of 50 mA cm⁻². (i) Comparison of mass activity and current density with other Pt catalysts.

dissolution of Ni atoms (Fig. S18b), which can optimize the coordination environment of Pt atoms and contribute to high activity and durability of PtNiP NWs [50,51]. The XPS result (Fig. S18c) shows that the oxidation state of P peak is weakened after stability tests, which is caused by the dissolution of phosphate in the electrolyte. The long-term cyclic voltammetry tests showed no obvious increase of overpotential for PtNiP NWs after 10,000 cycles (Fig. S19). The small potential increase will be further studied and modified in the future. In order to further highlight the excellent performance of PtNiP NWs, different Pt catalysts in references are displayed to compare the current density at -70 mV vs RHE. Impressively, the performance of PtNiP NWs still stands out in comparison with other works of Pt based catalysts (Fig. 4i) [23,34,52–58].

Density functional theory (DFT) calculations are applied to explore the mechanism of the excellent HER performance of PtNiP NWs in alkaline condition. Here we built up the Pt (1 1 1), PtNi (1 1 1), and PtNiP (1 1 1) to calculate their catalytic performance. After simulating and analyzing each step of HER reaction in alkaline condition, it was found that the excellent HER performance was due to the synergistic effect of Pt, Ni and P atoms in the ultrafine nanowires (Fig. 5a). The water molecules were firstly adsorbed on the Ni sites of PtNiP (1 1 1), and then the H₂O would obtain one electron to be dissociated into intermediate OH⁻ and H^{*} (Volmer step). Next step involves the OH⁻ transfers from Ni site to P site because the simulated result displays that the adsorption energy for OH⁻ on P sites is lower than that of Ni sites, which helps the dissociation of H₂O into OH⁻ and H^{*} [59]. At the same

time, H^{*} will diffuse to the nearby Pt atoms. Finally, two adjacent H^{*} will combine to produce hydrogen as discussed in the previous experiment (Tafel step).

The complete reaction energy diagram for water dissociation and hydrogen evolution are shown in Figs. 5b and S20. We found that Pt (1 1 1) surface has little adsorption ability for water molecules, directly leading to poor HER performance for Pt in alkaline conditions (Fig. S21). Fortunately, PtNiP (1 1 1) surface displays a much more favorable water adsorption energy (-0.12 eV) compare to 0.17 eV for PtNi (1 1 1) surface, suggesting that the water molecule could be readily adsorbed on surfaces of PtNiP (1 1 1) surface. As for water dissociation energy (ΔG_b), PtNiP (1 1 1) surface has a low water dissociation energy (0.48 eV) in comparison to 0.79 eV for PtNi (1 1 1) surface. Obviously, such a higher water dissociation energy clearly hinder the breaking the OH-H bond in adsorbed H₂O molecule to H^{*} and OH^{*}. Thus, the PtNiP (1 1 1) surface can promote both thermodynamic and kinetic process of H₂O molecular adsorption and dissociation, the adsorption and binding of H, which is consistent with the conclusion of our experiments.

Hence, Pt, Ni and P atoms play their roles in the catalytic system differently (Fig. 5c). Specifically, Ni atoms are conducive to the adsorption of water molecules. P atoms are helpful for the adsorption of OH⁻, which can accelerate the dissociation of H₂O. Finally, Pt atoms are excellent sites for the generation of H₂. The effective trilateral collaboration results in outstanding HER performance in alkaline condition.

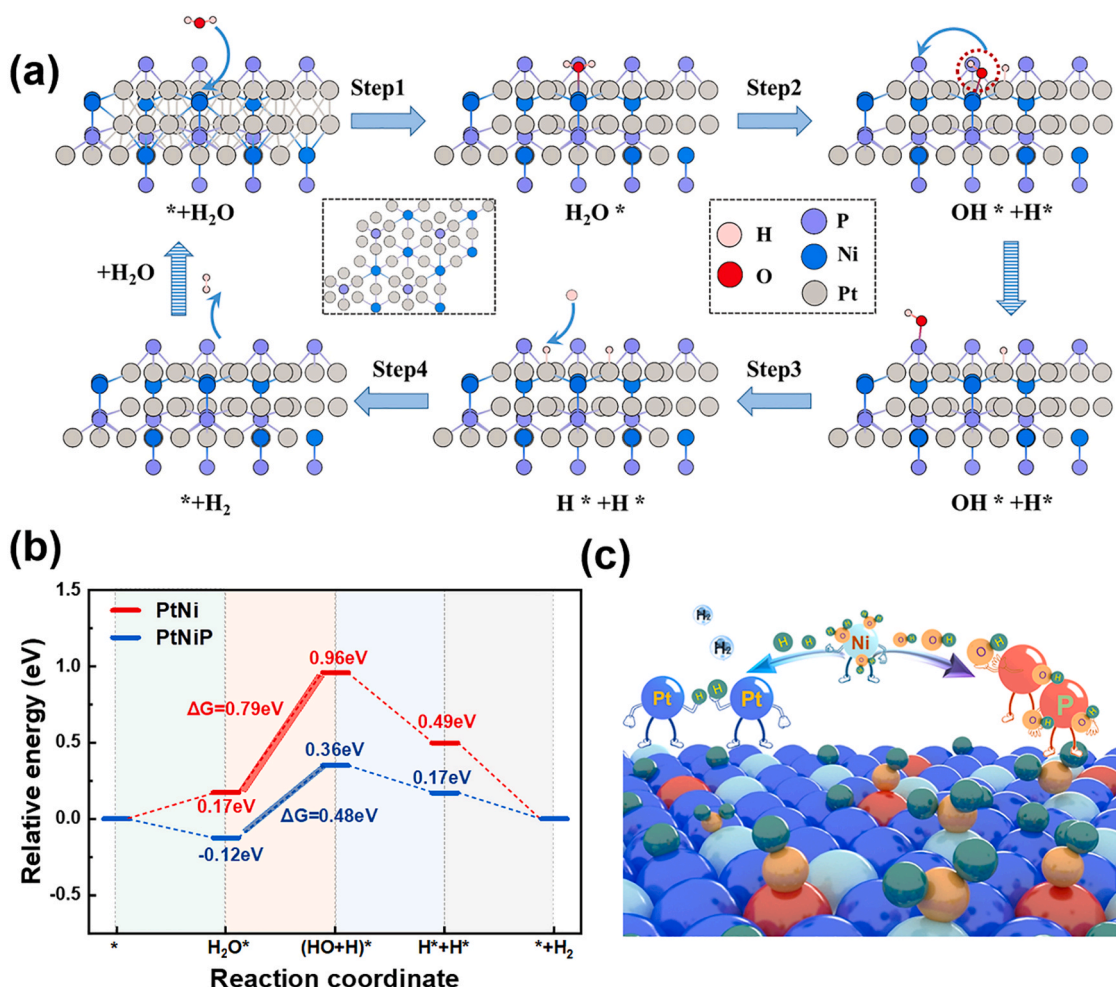


Fig. 5. (a) Reaction process schematic diagram of PtNiP NWs in alkaline condition. (b) Reaction free energy diagram of PtNi and PtNiP for whole HER process. (c) Schematic diagram of synergistic effect of Pt, Ni and P atoms.

4. Conclusion

In summary, we have successfully synthesized the ultrafine PtNiP NWs via a two-step hydrothermal reaction method. HAADF-STEM and EELS images reveal that both P and Ni are uniformly distributed in PtNiP nanowires. Impressively, the PtNiP NWs exhibit superior electrocatalytic activity toward HER under alkaline conditions, which can reach current density of 500 mA cm^{-2} only at the -0.153 V vs RHE and Tafel slop only 30 mV dec^{-1} . The DFT calculation results show synergistic effect of Pt, Ni and P atoms in nanowires, which significantly improved the kinetic processes of hydrogen evolution reaction in alkaline condition. Using heteroatoms to introduce synergistic effect will be an inspiring strategy to further improve the catalytic properties of Pt. This work could also be instructive and meaningful to design highly efficient and stable HER catalyst in alkaline condition.

CRediT authorship contribution statement

Qian Chen: Investigation, Data curation, Resources, Conceptualization, Methodology, Formal analysis, Writing – original draft. **Bo Wei:** Project administration, Software, Formal analysis, Writing – review & editing. **Yi Wei:** Visualization, Writing – review & editing. **Pengbo Zhai:** Formal analysis. **Wei Liu:** Methodology, **Xiaokang Gu:** Formal analysis. **Zhilin Yang:** Investigation, Resources. **Jinghan Zuo:** Formal analysis. **Ruifeng Zhang:** Validation, Investigation, Writing – review & editing. **Yongji Gong:** Funding acquisition, Project administration, Resources, Supervision, Validation, Writing – review & editing.

Declaration of Competing Interest

The authors declare that they have no known competing financial interests or personal relationships that could have appeared to influence the work reported in this paper.

Acknowledgments

This work was supported by the National Natural Science Foundation of China (51872012), the Key Technologies Research and Development Program of China (Grant No. 2018YFA0306900).

Appendix A. Supporting information

Supplementary data associated with this article can be found in the online version at [doi:10.1016/j.apcatb.2021.120754](https://doi.org/10.1016/j.apcatb.2021.120754).

References

- [1] T.F. Jaramillo, K.P. Jørgensen, J. Bonde, J.H. Nielsen, S. Hørch, I. Chorkendorff, Identification of active edge sites for electrochemical H_2 evolution from MoS_2 nanocatalysts, *Science* 317 (2007) 100–102.
- [2] R. Subbaraman, D. Tripkovic, D. Strmcnik, K.-C. Chang, M. Uchiumura, A. P. Paulikas, V. Stamenkovic, N.M. Markovic, Enhancing hydrogen evolution activity in water splitting by tailoring $\text{Li}-\text{Ni}(\text{OH})_2\text{-Pt}$ interfaces, *Science* 334 (2011) 1256–1260.
- [3] J.D. Holladay, J. Hu, D.L. King, Y. Wang, An overview of hydrogen production technologies, *Catal. Today* 139 (2009) 244–260.

- [4] T. Ling, T. Zhang, B. Ge, L. Han, L. Zheng, F. Lin, Z. Xu, W.-B. Hu, X.-W. Du, K. Davey, S.-Z. Qiao, Well-dispersed nickel- and zinc-tailored electronic structure of a transition metal oxide for highly active alkaline hydrogen evolution reaction, *Adv. Mater.* 31 (2019), 1807771.
- [5] Y. Li, M. Lu, Y. Wu, H. Xu, J. Gao, J. Yao, Trimetallic metal-organic framework derived carbon-based nanoflower electrocatalysts for efficient overall water splitting, *Adv. Mater. Interfaces* 6 (2019), 1900290.
- [6] J.-X. Feng, H. Xu, Y.-T. Dong, X.-F. Lu, Y.-X. Tong, G.-R. Li, Efficient hydrogen evolution electrocatalysis using cobalt nanotubes decorated with titanium dioxide nanodots, *Angew. Chem. Int. Ed. Engl.* 56 (2017) 2960–2964.
- [7] J. Yang, A.R. Mohamad, Y. Wang, R. Fullon, X. Song, F. Zhao, I. Bozkurt, M. Augustin, E.J.G. Santos, H.S. Shin, W. Zhang, D. Voirey, H.Y. Jeong, M. Chhowalla, Ultrahigh-current-density niobium disulfide catalysts for hydrogen evolution, *Nat. Mater.* 18 (2019) 1309–1314.
- [8] W. Yang, S. Zhang, Q. Chen, C. Zhang, Y. Wei, H. Jiang, Y. Lin, M. Zhao, Q. He, X. Wang, Y. Du, L. Song, S. Yang, A. Nie, X. Zou, Y. Gong, Conversion of intercalated MoO₃ to multi-heteroatoms-doped MoS₂ with high hydrogen evolution activity, *Adv. Mater.* 32 (2020), 2001167.
- [9] H.J. Haifeng Que, X. Wang, P. Zhai, L. Meng, P. Zhang, Y. Gong, *Acta Phys. -Chim. Sin.* 37 (2021), 2010051.
- [10] J.-H. Zuo, Y.-J. Gong, Applications of transition-metal sulfides in the cathodes of lithium-sulfur batteries, *Tungsten* 2 (2020) 134–146.
- [11] L. Yu, S. Song, B. McElhenny, F. Ding, D. Luo, Y. Yu, S. Chen, Z. Ren, A universal synthesis strategy to make metal nitride electrocatalysts for hydrogen evolution reaction, *J. Mater. Chem. A* 7 (2019) 19728–19732.
- [12] J. Lai, B. Huang, Y. Chao, X. Chen, S. Guo, Strongly coupled nickel-cobalt nitrides/carbon hybrid nanocages with Pt-like activity for hydrogen evolution catalysis, *Adv. Mater.* 31 (2019), 1805541.
- [13] J.-X. Feng, S.-Y. Tong, Y.-X. Tong, G.-R. Li, Pt-like hydrogen evolution electrocatalysis on PANI/CoP hybrid nanowires by weakening the shackles of hydrogen ions on the surfaces of catalysts, *J. Am. Chem. Soc.* 140 (2018) 5118–5126.
- [14] Y. Wei, R.A. Soomro, X. Xie, B. Xu, Mediastinum metastasis in a post-surgical pancreatic cancer patient successfully confirmed with endoscopic ultrasonography, *World J. Emerg. Med.* 12 (2021) 244–246.
- [15] L. Chen, K. Chen, S. Zhu, Transition-metal-catalyzed intramolecular nucleophilic addition of carbonyl groups to alkynes, *Chem* 4 (2018) 1208–1262.
- [16] J. Zhang, Y. Zhao, X. Guo, C. Chen, C.-L. Dong, R.-S. Liu, C.-P. Han, Y. Li, Y. Gogotsi, G. Wang, Single platinum atoms immobilized on an MXene as an efficient catalyst for the hydrogen evolution reaction, *Nat. Catal.* 1 (2018) 985–992.
- [17] X. Li, X. Lv, X. Sun, C. Yang, Y.-Z. Zheng, L. Yang, S. Li, X. Tao, Edge-oriented, high-percentage 1T'-phase MoS₂ nanosheets stabilize Ti₃C₂ MXene for efficient electrocatalytic hydrogen evolution, *Appl. Catal. B: Environ.* 284 (2021), 119708.
- [18] B. Zhou, C. Zhu, Z. Wu, E. Stavitski, Y.H. Lui, T.-H. Kim, H. Liu, L. Huang, X. Luan, L. Zhou, K. Jiang, W. Huang, S. Hu, H. Wang, J.S. Francisco, Integrating Rh species with NiFe-layered double hydroxide for overall water splitting, *Nano Lett.* 20 (2020) 136–144.
- [19] D. Wang, Q. Li, C. Han, Q. Lu, Z. Xing, X. Yang, Atomic and electronic modulation of self-supported nickel-vanadium layered double hydroxide to accelerate water splitting kinetics, *Nat. Commun.* 10 (2019) 3899.
- [20] Y. Zhao, Y. Gao, Z. Chen, Z. Li, T. Ma, Z. Wu, L. Wang, Trifunctional Pt coupled with NiFe hydroxide synthesized via corrosion engineering to boost the cleavage of water molecule for alkaline water-splitting, *Appl. Catal. B: Environ.* 297 (2021), 120395.
- [21] P. Zhai, X. Gu, Y. Wei, J. Zuo, Q. Chen, W. Liu, H. Jiang, X. Wang, Y. Gong, Enhanced mass transfer in three-dimensional single-atom nickel catalyst with open-pore structure for highly efficient CO₂ electrolysis, *J. Energy Chem.* 62 (2021) 43–50.
- [22] J.-X. Feng, H. Xu, S.-H. Ye, G. Ouyang, Y.-X. Tong, G.-R. Li, Silica-polypropylene hybrids as high-performance metal-free electrocatalysts for the hydrogen evolution reaction in neutral media, *Angew. Chem. Int. Ed. Engl.* 56 (2017) 8120–8124.
- [23] Z. Zhao, H. Liu, W. Gao, W. Xue, Z. Liu, J. Huang, X. Pan, Y. Huang, Surface-engineered PtNi-O nanostructure with record-high performance for electrocatalytic hydrogen evolution reaction, *J. Am. Chem. Soc.* 140 (2018) 9046–9050.
- [24] T.F. Jaramillo, K.P. Jørgensen, J. Bonde, J.H. Nielsen, S. Hørch, I. Chorkendorff, Identification of active edge sites for electrochemical H₂ evolution from MoS₂ nanocatalysts, *Science* 317 (2007) 100–102.
- [25] J. Greeley, M. Mavrikakis, Alloy catalysts designed from first principles, *Nat. Mater.* 3 (2004) 810–815.
- [26] J. Lai, F. Lin, Y. Tang, P. Zhou, Y. Chao, Y. Zhang, S. Guo, Efficient bifunctional polyalcohol oxidation and oxygen reduction electrocatalysts enabled by ultrathin PtPDM (M = Ni, Fe, Co) nanosheets, *Adv. Energy Mater.* 9 (2019), 1800684.
- [27] Y. Zhang, X.-L. Yuan, F.-L. Lyu, X.-C. Wang, X.-J. Jiang, M.-H. Cao, Q. Zhang, Facile one-step synthesis of PdPb nanochains for high-performance electrocatalytic ethanol oxidation, *Rare Met.* 39 (2020) 792–799.
- [28] M. Yao, B. Wang, B. Sun, L. Luo, Y. Chen, J. Wang, N. Wang, S. Komarneni, X. Niu, W. Hu, Rational design of self-supported Cu@WC core-shell mesoporous nanowires for pH-universal hydrogen evolution reaction, *Appl. Catal. B: Environ.* 280 (2021), 119451.
- [29] H. Lv, X. Chen, D. Xu, Y. Hu, H. Zheng, S.L. Suib, B. Liu, Ultrathin PdPt bimetallic nanowires with enhanced electrocatalytic performance for hydrogen evolution reaction, *Appl. Catal. B: Environ.* 238 (2018) 525–532.
- [30] L.-X. Ding, A.-L. Wang, G.-R. Li, Z.-Q. Liu, W.-X. Zhao, C.-Y. Su, Y.-X. Tong, Porous Pt-Ni-P composite nanotube arrays: highly electroactive and durable catalysts for methanol electrooxidation, *J. Am. Chem. Soc.* 134 (2012) 5730–5733.
- [31] X.-Q. Cao, J. Zhou, S. Li, G.-W. Qin, Long non-coding RNA in bladder cancer, *Clin. Chim. Acta; Int. J. Clin. Chem.* 503 (2020) 113–121.
- [32] J.R. Kitchin, J.K. Nørskov, M.A. Barteau, J.G. Chen, Modification of the surface electronic and chemical properties of Pt(111) by subsurface 3d transition metals, *J. Chem. Phys.* 120 (2004) 10240–10246.
- [33] Y. Li, Y. Sun, Y. Qin, W. Zhang, L. Wang, M. Luo, H. Yang, S. Guo, Recent advances on water-splitting electrocatalysis mediated by noble-metal-based nanostructured materials, *Adv. Energy Mater.* 10 (2020), 1903120.
- [34] Y. Xie, J. Cai, Y. Wu, Y. Zang, X. Zheng, J. Ye, P. Cui, S. Niu, Y. Liu, J. Zhu, X. Liu, G. Wang, Y. Qian, Boosting water dissociation kinetics on Pt-Ni nanowires by N-induced orbital tuning, *Adv. Mater.* 31 (2019), 1807780.
- [35] B.Y. Xia, H.B. Wu, Y. Yan, X.W. Lou, X. Wang, Ultrathin and ultralong single-crystal platinum nanowire assemblies with highly stable electrocatalytic activity, *J. Am. Chem. Soc.* 135 (2013) 9480–9485.
- [36] X. Zhu, L. Huang, M. Wei, P. Tsiakaras, P.K. Shen, Highly stable Pt-Co nanodendrite in nanoframe with Pt skin structured catalyst for oxygen reduction electrocatalysis, *Appl. Catal. B: Environ.* 281 (2021), 119460.
- [37] P. Wang, W. Nong, Y. Li, H. Cui, C. Wang, Strengthening nitrogen affinity on CuAu@Cu core-shell nanoparticles with ultrathin Cu skin via strain engineering and ligand effect for boosting nitrogen reduction reaction, *Appl. Catal. B: Environ.* 288 (2021), 119999.
- [38] F. Lv, W. Zhang, M. Sun, F. Lin, T. Wu, P. Zhou, W. Yang, P. Gao, B. Huang, S. Guo, Au clusters on Pd nanosheets selectively switch the pathway of ethanol electrooxidation: amorphous/crystalline interface matters, *Adv. Energy Mater.* 11 (2021), 2100187.
- [39] Y. Wen, J. Qi, D. Zhao, J. Liu, P. Wei, X. Kang, X. Li, O doping hierarchical NiCoP/Ni₂P hybrid with modulated electron density for efficient alkaline hydrogen evolution reaction, *Appl. Catal. B: Environ.* 293 (2021), 120196.
- [40] A. Ruban, B. Hammer, P. Stoltze, H.L. Skriver, J.K. Nørskov, Surface electronic structure and reactivity of transition and noble metals, *Communication presented at the First Francoqui Colloquium, Brussels, 19–20 February 1996*, *J. Mol. Catal. A: Chem.* 115 (1997) 421–429.
- [41] B. Hammer, J.K. Nørskov, Why gold is the noblest of all the metals, *Nature* 376 (1995) 238–240.
- [42] T. Liu, A. Li, C. Wang, W. Zhou, S. Liu, L. Guo, Interfacial electron transfer of Ni₂P-Ni₂P polymorphs inducing enhanced electrochemical properties, *Adv. Mater.* 30 (2018), 1803590.
- [43] M. Jin, X. Zhang, R. Shi, Q. Lian, S. Niu, O. Peng, Q. Wang, C. Cheng, Hierarchical CoP@Ni₂P catalysts for pH-universal hydrogen evolution at high current density, *Appl. Catal. B: Environ.* 296 (2021), 120350.
- [44] Q. Liu, J. Tian, W. Cui, P. Jiang, N. Cheng, A.M. Asiri, X. Sun, Carbon nanotubes decorated with CoP nanocrystals: a highly active non-noble-metal nanohybrid electrocatalyst for hydrogen evolution, *Angew. Chem. Int. Ed. Engl.* 53 (2014) 6710–6714.
- [45] J. Mao, W. Chen, D. He, J. Wan, J. Pei, J. Dong, Y. Wang, P. An, Z. Jin, W. Xing, H. Tang, Z. Zhuang, X. Liang, Y. Huang, G. Zhou, L. Wang, D. Wang, Y. Li, Design of ultrathin Pt-Mo-Ni nanowire catalysts for ethanol electrooxidation, *Sci. Adv.* 3 (2017), 1603068.
- [46] B.-J. Hwang, L.S. Sarma, J.-M. Chen, C.-H. Chen, S.-C. Shih, G.-R. Wang, D.-G. Liu, J.-F. Lee, M.-T. Tang, Structural models and atomic distribution of bimetallic nanoparticles as investigated by X-ray absorption spectroscopy, *J. Am. Chem. Soc.* 127 (2005) 11140–11145.
- [47] Y. Wang, L. Chen, X. Yu, Y. Wang, G. Zheng, Superb alkaline hydrogen evolution and simultaneous electricity generation by Pt-decorated Ni₃N nanosheets, *Adv. Energy Mater.* 7 (2017), 1601390.
- [48] T. Shinagawa, A.T. Garcia-Esparza, K. Takanabe, Insight on Tafel slopes from a microkinetic analysis of aqueous electrocatalysis for energy conversion, *Sci. Rep.* 5 (2015) 13801.
- [49] J. Mahmood, F. Li, S.-M. Jung, M.S. Okayay, I. Ahmad, S.-J. Kim, N. Park, H. Y. Jeong, J.-B. Baek, An efficient and pH-universal ruthenium-based catalyst for the hydrogen evolution reaction, *Nat. Nanotechnol.* 12 (2017) 441–446.
- [50] M. Li, K. Duanmu, C. Wan, T. Cheng, L. Zhang, S. Dai, W. Chen, Z. Zhao, P. Li, H. Fei, Y. Zhu, R. Yu, J. Luo, K. Zhang, Z. Lin, M. Ding, J. Huang, H. Sun, J. Guo, X. Pan, W.A. Goddard, P. Sautet, Y. Huang, X. Duan, Single-atom tailoring of platinum nanocatalysts for high-performance multifunctional electrocatalysis, *Nat. Catal.* 2 (2019) 495–503.
- [51] M. Gong, Z. Deng, D. Xiao, L. Han, T. Zhao, Y. Lu, T. Shen, X. Liu, R. Lin, T. Huang, G. Zhou, H. Xin, D. Wang, One-nanometer-thick Pt₃Ni bimetallic alloy nanowires advanced oxygen reduction reaction: integrating multiple advantages into one catalyst, *ACS Catal.* 9 (2019) 4488–4494.
- [52] S.W. Jang, S. Dutta, A. Kumar, Y.-R. Hong, H. Kang, S. Lee, S. Ryu, W. Choi, I. S. Lee, Holey Pt nanosheets on NiFe-hydroxide laminates: synergistically enhanced electrocatalytic 2D interface toward hydrogen evolution reaction, *ACS Nano* 14 (2020) 10578–10588.
- [53] Z. Liu, J. Qi, M. Liu, S. Zhang, Q. Fan, H. Liu, K. Liu, H. Zheng, Y. Yin, C. Gao, Aqueous synthesis of ultrathin platinum/non-noble metal alloy nanowires for enhanced hydrogen evolution activity, *Angew. Chem. Int. Ed. Engl.* 57 (2018) 11678–11682.
- [54] P. Wang, X. Zhang, J. Zhang, S. Wan, S. Guo, G. Lu, J. Yao, X. Huang, Precise tuning in platinum-nickel/nickel sulfide interface nanowires for synergistic hydrogen evolution catalysis, *Nat. Commun.* 8 (2017) 14580.
- [55] P. Wang, K. Jiang, G. Wang, J. Yao, X. Huang, Phase and interface engineering of platinum-nickel nanowires for efficient electrochemical hydrogen evolution, *Angew. Chem. Int. Ed.* 55 (2016) 12859–12863.

- [56] C. Guo, Y. Jiao, Y. Zheng, J. Luo, K. Davey, S.-Z. Qiao, Intermediate modulation on noble metal hybridized to 2D metal-organic framework for accelerated water electrocatalysis, *Chem* 5 (2019) 2429–2441.
- [57] Z. Zhang, G. Liu, X. Cui, B. Chen, Y. Zhu, Y. Gong, F. Saleem, S. Xi, Y. Du, A. Borgna, Z. Lai, Q. Zhang, B. Li, Y. Zong, Y. Han, L. Gu, H. Zhang, Crystal phase and architecture engineering of lotus-thalamus-shaped Pt-Ni anisotropic superstructures for highly efficient electrochemical hydrogen evolution, *Adv. Mater.* 30 (2018), 1801741.
- [58] M. Lao, K. Rui, G. Zhao, P. Cui, X. Zheng, S.X. Dou, W. Sun, Platinum/nickel bicarbonate heterostructures towards accelerated hydrogen evolution under alkaline conditions, *Angew. Chem. Int. Ed. Engl.* 58 (2019) 5432–5437.
- [59] J.L.C. Fajin, M.N.D.S. Cordeiro, J.R.B. Gomes, Density functional theory study of the water dissociation on platinum surfaces: general trends, *J. Phys. Chem. A* 118 (2014) 5832–5840.